Structure of krypton isotopes within the interacting boson model derived from the Gogny energy density functional

K. Nomura,[1,2] R. Rodríguez-Guzmán,[3] Y. M. Humadi,[3] L. M. Robledo,[4] and H. Abusara[5]
[1]*Physics Department, Faculty of Science, University of Zagreb, HR-10000 Zagreb, Croatia*
[2]*Center for Computational Sciences, University of Tsukuba, Tsukuba 305-8577, Japan*
[3]*Physics Department, Kuwait University, 13060 Kuwait, Kuwait*
[4]*Departamento de Física Teórica, Universidad Autónoma de Madrid, E-28049 Madrid, Spain*
[5]*Department of Physics, Birzeit University, Birzeit, Palestine*
(Received 2 July 2017; published 8 September 2017)

The evolution and coexistence of the nuclear shapes as well as the corresponding low-lying collective states and electromagnetic transition rates are investigated along the krypton isotopic chain within the framework of the interacting boson model (IBM). The IBM Hamiltonian is determined through mean-field calculations based on the several parametrizations of the Gogny energy density functional and the relativistic mean-field Lagrangian. The mean-field energy surfaces, as functions of the axial β and triaxial γ quadrupole deformations, are mapped onto the expectation value of the interacting-boson Hamiltonian that explicitly includes the particle-hole excitations. The resulting boson Hamiltonian is then used to compute low-energy excitation spectra as well as $E2$ and $E0$ transition probabilities for $^{70-100}$Kr. Our results point to a number of examples of prolate-oblate shape transitions and coexistence both on the neutron-deficient and neutron-rich sides. A reasonable agreement with the available experimental data is obtained for the considered nuclear properties.

DOI: 10.1103/PhysRevC.96.034310

I. INTRODUCTION

The low-lying structure of Kr isotopes is characterized by a rich variety of shape phenomena, such as shape transitions when neutron number is varied [1,2] as well as shape coexistence and mixing [3]. On the neutron-deficient side, especially in the case of isotopes with approximately the same number of protons and neutrons, the experimental evidence [4] regarding the emergence of prolate-oblate shape coexistence and mixing has already been studied using different theoretical frameworks [4–9]. Low-lying excited 0^+ states have been observed for some Kr nuclei, e.g., $^{72-78}$Kr. Those states have been associated with intruder excitations [3].

In the last few years, it has become possible to access neutron-rich Kr nuclei experimentally [10–15]. Even those isotopes beyond the neutron number $N \approx 60$ have been experimentally studied, as reported quite recently in Refs. [14,15], where the spectroscopy of the radioactive isotopes ^{96,98,100}Kr is analyzed. The structural evolution in neutron-rich nuclei with mass number $A \approx 100$ is rather sensitive to the underlying shell structure, and such experimental information is quite useful to deepen our understanding of it and offers the possibility to learn about unique features related to shape transitions in neutron-rich Kr isotopes. For instance, in contrast to its neighboring neutron-rich Sr and Zr nuclei where the shape transition is suggested to take place rather rapidly around $N = 60$ [16–18], the onset of deformation is shown to emerge much more moderately along the Kr isotopic chain [11,12,14].

From a theoretical point of view, the large-scale shell model [19] and the nuclear energy density functional (EDF) [20] approaches are among the most popular microscopic nuclear structure models for medium-heavy and heavy nuclei. The former allows direct access to the spectroscopic properties via the diagonalization of the Hamiltonian matrix defined in the corresponding configuration space. However, in open-shell regions with increasing number of valence nucleons, the dimension of the shell-model matrix becomes exceedingly large, making a systematic investigation of the nuclear spectroscopy less tractable. On the other hand, the EDF framework allows the systematic study of several nuclear properties all over the nuclear chart. A number of self-consistent mean-field (SCMF) calculations with both nonrelativistic [20] and relativistic [21,22] EDFs have so far been performed to investigate structural phenomena in atomic nuclei. Nevertheless, a more quantitative analysis of shape transitions requires the extension of the mean-field framework so as to include beyond-mean-field correlations associated with the restoration of broken symmetries and/or fluctuations in the collective parameters within the symmetry-projected generator coordinate method (GCM) (see, for example, [20,22,23]). Though quite robust, the method becomes increasingly difficult to implement from a computational point of view in the case of heavy nuclei and/or when several collective coordinates have to be considered in the symmetry-projected GCM ansatz.

To alleviate the computational effort required in symmetry-projected GCM configuration mixing calculations, several approximations have already been employed. Among them we mention here the five-dimensional collective Hamiltonian (5DCH) approach, based on both nonrelativistic [24] and relativistic [22] EDFs, and the fermion-to-boson mapping procedure that allows one to build an algebraic model of interacting bosons [25] starting from a given EDF. In this study, we resort to the latter approach [25] and use the microscopic energy surface of a given nucleus, obtained via constrained mean-field calculations [26], as input to a mapping procedure involving the intrinsic wave function of the boson system, taking into account particle-hole excitations. This mapping procedure allows the determination of the

parameters of the corresponding (bosonic) IBM Hamiltonian that is subsequently used to compute the excitation spectra and electromagnetic transition rates for a give nuclear system. At variance with the phenomenological IBM calculations, where the parameters of the Hamiltonian are fitted to reproduce spectroscopic data, within the already mentioned fermion-to-boson mapping procedure [25] the corresponding IBM Hamiltonian is obtained from microscopic EDF calculations and, therefore, the method can be extrapolated to regions of the nuclear chart where experimental data are scarce or even not available. Several applications of the fermion-to-boson mapping procedure have been reported in the literature. For instance, it was recently employed to describe shape transitions and shape coexistence in Ru, Mo, Zr, and Sr isotopes with mass number $A \approx 100$ [27] as well as for neutron-rich Ge and Se nuclei with $70 \leqslant A \leqslant 90$ [28].

In this study, we have resorted to the parametrization D1M [29] of the Gogny EDF to obtain, via mean-field calculations, the required microscopic input used to build the IBM Hamiltonian. To examine the robustness of our fermion-to-boson mapping procedure with respect to the underlying EDF, calculations have been performed with two other parametrizations of the Gogny EDF, i.e., D1S [30] and D1N [31]. Furthermore, mean-field calculations have also been carried out with the density-dependent meson-exchange (DD-ME2) [32] and point-coupling (DD-PC1) [33] relativistic EDFs. Nevertheless, in our discussions we will mainly focus on the results obtained with the Gogny-D1M EDF since, as will be shown, the results to be presented later on in this study do not depend significantly on the underlying EDF employed in the mapping procedure.

The paper is organized as follows. In Sec. II, we briefly outline the fermion-to-boson mapping procedure employed in this work to study the isotopes $^{70–100}$Kr. The results of our calculations are presented in Sec. III. First, in Sec. III A, we discuss the microscopic energy surfaces obtained at the mean-field level as well as the mapped IBM ones. The IBM parameters derived via the mapping procedure and the configurations employed in the calculations are presented in Sec. III B. In Secs. III C and III D, we turn our attention to spectroscopic properties such as the systematics of the energy spectra and the transition rates predicted in our calculations as well as to the comparison with the available experimental data. The detailed spectroscopy of a selected sample of Kr isotopes is discussed in Sec. III E. In Sec. III F, we consider the sensitivity of the results with respect to the underlying EDF used in the mapping procedure. Finally, Sec. IV is devoted to concluding remarks and work perspectives.

II. DESCRIPTION OF THE MODEL

In this section, we briefly outline the fermion-to-boson mapping procedure employed in this work. For a more detailed account, the reader is referred to [27,28] and references therein.

A. SCMF calculations

The first step in our procedure is to perform a set of constrained SCMF calculations, within the Hartree-Fock-Bogoliubov (HFB) method and based on the Gogny-D1M EDF [34]. We have also carried out mean-field calculations with the parametrizations D1S [30] and D1N [31] of the Gogny EDF as well as with the relativistic DD-ME2 [32] and DD-PC1 [33] EDFs. In this way we obtain the HFB deformation energy surfaces parametrized by the usual quadrupole shape degrees of freedom β and γ [35]. Here, we have used constraints on the operators $\hat{Q}_{20}$ and $\hat{Q}_{22}$. They are related to the deformation parameters β and γ through the relations $\beta = \sqrt{4\pi/5}\sqrt{\langle\hat{Q}_{20}\rangle^2 + \langle\hat{Q}_{22}\rangle^2}/\langle r^2\rangle$ and $\gamma = \arctan(\langle\hat{Q}_{22}\rangle/\langle\hat{Q}_{20}\rangle)$, respectively. In the previous expressions, $\langle r^2\rangle$ denotes the mean-square radius obtained from the corresponding HFB state.

B. IBM framework

The building blocks of the IBM system, that predominantly determine the low-energy quadrupole collective states, are the $J^\pi = 0^+$ (s) and 2^+ (d) bosons which represent the collective $J^\pi = 0^+$ and 2^+ pairs of valence nucleons, respectively [36,37]. Therefore, the number of bosons n_b equals that of pairs of valence nucleons (particle or hole) [36,37]. The boson Hamiltonian is diagonalized in a given valence space (one major shell). In the present work, we use the same model space for the boson system as in our previous study [28], i.e, the proton $Z = 28$–50 major shell and the neutron $N = 28$–50 (for $^{70–86}$Kr) and $N = 50$–82 (for $^{88–100}$Kr) major shells. For the sake of simplicity, no distinction is made between proton and neutron bosons.

For many of the studied Kr isotopes, the Gogny-D1M HFB energy surfaces exhibit more than one minimum, reflecting a pronounced competition between different intrinsic configurations. Previous IBM calculations already suggest that the low-lying 0_2^+ state in neutron-deficient Kr isotopes, as well as in the neighboring Se and Ge nuclei, could arise from particle-hole excitations and therefore have an intrinsic structure different from the one of the ground state [38–40]. As a consequence, to describe the structure of Kr isotopes, it is necessary to extend the IBM framework so as to include the effect of particle-hole excitations. To this end, we have adapted the configuration mixing technique developed by Duval and Barrett [41,42]. Within this context, shell-model-like $2k$-particle-$2k$-hole ($k = 0,1,2,\ldots$) configurations are associated with boson spaces comprising $n_b + 2k$ bosons. The different boson subspaces are allowed to mix via an interaction term that does not preserve the boson number. The configuration-mixing IBM Hamiltonian is then diagonalized in the space $[n_b] \oplus [n_b + 2] \oplus [n_b + 4] \oplus \cdots$, with $[n_b + 2k]$ being the unperturbed boson subspace. As in several earlier calculations made in the same mass region (e.g., [28,39,40]), we have considered proton particle-hole excitations across the $Z = 28$ major shell gap. Moreover, as will be shown below, the Gogny-HFB energy surfaces display up to three mean-field minima. Those minima are sufficiently well defined so as to constrain the corresponding unperturbed IBM Hamiltonian and, therefore, we consider up to three configurations: the normal 0p-0h as well as the intruder 2p-2h and 4p-4h excitations.

The configuration mixing IBM Hamiltonian employed in this work reads

$$\hat{H} = \hat{H}_0 + (\hat{H}_1 + \Delta_1) + (\hat{H}_2 + \Delta_2) + \hat{H}^{\rm mix}_{01} + \hat{H}^{\rm mix}_{12}, \quad (1)$$

where $\hat{H}_k$ ($k = 0,1,2$) is the Hamiltonian for the unperturbed configuration space $[n_b + 2k]$ while $\hat{H}^{\rm mix}_{kk+1}$ ($k = 0,1$) stands for the interaction mixing $[n_b + 2k]$ and $[n_b + 2(k+1)]$ spaces. In Eq. (1), Δ_1 and Δ_2 represent the energy needed to excite one and two bosons from one major shell to the next.

For each configuration space, we have employed the simplest form of the IBM-1 Hamiltonian that still simulates the essential ingredients of the low-energy quadrupole dynamics, i.e.,

$$\hat{H}_k = \epsilon_k \hat{n}_d + \kappa_k \hat{Q} \cdot \hat{Q} + \kappa'_k \hat{V}_{ddd}. \quad (2)$$

The first term in Eq. (2) is the d-boson number operator, with ϵ_k ($k = 0,1,2$) being the single d-boson energy in the $[n_b + 2k]$ space. The second term represents the quadrupole-quadrupole interaction with strength parameter κ_k. The quadrupole operator $\hat{Q}$ reads $\hat{Q} = s^\dagger \tilde{d} + d^\dagger s + \chi_k [d^\dagger \times \tilde{d}]^{(2)}$, where χ_k is a parameter. On the other hand, the third term stands for the most relevant three-body interaction with strength κ'_k. This term is required to describe γ-soft systems [43,44] and takes the form

$$\hat{V}_{ddd} = [[d^\dagger \times d^\dagger \times d^\dagger]^{(3)} \times [\tilde{d} \times \tilde{d} \times \tilde{d}]^{(3)}]^{(0)}. \quad (3)$$

The mixing interaction $\hat{H}^{\rm mix}_{kk+1}$ ($k = 0$ or 1) reads

$$\hat{H}^{\rm mix}_{kk+1} = \omega^s_k s^\dagger s^\dagger + \omega^d_k d^\dagger \cdot d^\dagger + ({\rm H.c.}), \quad (4)$$

where ω^s_k and ω^d_k are strength parameters. For simplicity, we have assumed $\omega^s_k = \omega^d_k \equiv \omega_k$. There is no direct coupling between the $[n_b]$ and $[n_b + 4]$ spaces with the two-body interactions.

To associate the configuration-mixing IBM Hamiltonian of Eq. (1) with the corresponding Gogny-HFB energy surface, an extended boson coherent state has been introduced [45]:

$$|n_0,(\beta_0,\gamma_0)\rangle \oplus |n_1,(\beta_1,\gamma_1)\rangle \oplus |n_2,(\beta_2,\gamma_2)\rangle, \quad (5)$$

where $n_k = n_b + 2k$ ($k = 0,1,2$). For each unperturbed configuration space $|n_k,(\beta_k,\gamma_k)\rangle$ ($k = 0,1,2$), the coherent state is taken in the form

$$|n_k,(\beta_k,\gamma_k)\rangle = \frac{1}{\sqrt{n_k!}} \Big(s^\dagger + \beta_k \cos\gamma_k d^\dagger_0 + \frac{1}{\sqrt{2}} \beta_k \sin\gamma_k (d^\dagger_{+2} + d^\dagger_{-2}) \Big)^{n_k} |0\rangle, \quad (6)$$

where $|0\rangle$ denotes the inert core. For each unperturbed configuration $[n_b + 2k]$, the boson analogs of the quadrupole deformation parameters β and γ are denoted by β_k and γ_k, respectively [35]. They are assumed to be in correspondence with the ones of the the Gogny-HFB by means of a linear dependence with $\beta_k = C_k \beta$ and $\gamma_k = \gamma$. The constants C_k are also determined by fitting the (fermionic) Gogny-HFB energy surface to the (bosonic) IBM one by requiring that the position of the minimum is reproduced for each unperturbed configuration.

The expectation value of the total Hamiltonian $\hat{H}$ in the coherent state Eq. (5) leads to a 3×3 matrix [45]:

$$\mathcal{E} = \begin{pmatrix} E_0(\beta,\gamma) & \Omega_{01}(\beta) & 0 \\ \Omega_{01}(\beta) & E_1(\beta,\gamma) + \Delta_1 & \Omega_{12}(\beta) \\ 0 & \Omega_{12}(\beta) & E_2(\beta,\gamma) + \Delta_2 \end{pmatrix}, \quad (7)$$

with diagonal and off-diagonal elements accounting for the expectation values of the unperturbed and mixing terms, respectively. The three eigenvalues of $\mathcal{E}$ correspond to specific energy surfaces. It is customary to take the lowest-energy one [45] as the IBM energy surface. Both $E_k(\beta,\gamma)$ and $\Omega_{kk+1}(\beta)$ are computed analytically. Their expressions can be found in Ref. [28].

C. Derivation of the IBM parameters: The fitting procedure

The Hamiltonian in Eq. (1) contains 16 parameters. They have been determined along the following lines:

(i) The unperturbed Hamiltonians are determined by using the procedure of Refs. [25,27,46]: each diagonal matrix element $E_k(\beta,\gamma)$ in Eq. (7) is fitted to reproduce the topology of the Gogny-HFB energy surface in the neighborhood of the corresponding minimum. The normal $[n_b]$ configuration is assigned to the HFB minimum with the smallest β deformation, the $[n_b + 2]$ configuration is assigned to the minimum with the second smallest β deformation, and the $[n_b + 4]$ configuration is associated to the minimum with the third smallest β deformation. In this way, each unperturbed Hamiltonian is determined independently.

(ii) The energy offset Δ_{k+1} ($k = 0,1$) is determined so that the energy difference between the two minima of the Gogny-HFB energy surface, associated with the $[n_b + 2k]$ and $[n_b + 2(k+1)]$ configurations, is reproduced.

(iii) The strength parameter ω_{kk+1} ($k = 0,1$) of the mixing interaction term $\hat{H}^{\rm mix}_{kk+1}$ is determined so as to reproduce the shapes of the barriers between the minima corresponding to the $[n_b + 2k]$ and $[n_b + 2(k+1)]$ configurations [47,48]. Steps (ii) and (iii) are repeated until the best match is obtained between the HFB and IBM energy surfaces.

We have assumed that the boson-number dependence of the κ parameter is consistent with earlier IBM calculations [25,37], i.e., κ decreases in magnitude as a function of n_b, to determine the parameters of the unperturbed Hamiltonians. In step (i), the link of the unperturbed configurations with the deformed minima is based on the assumption that the interpretation of shape coexistence in the neutron-deficient lead region [49–51] also holds here. In the case of mercury nuclei, for instance, the 0^+_1 ground state is associated with a weakly deformed oblate shape and the intruder 0^+_2 state with a prolate shape with a larger β deformation [49,51]. Obviously, this assumption can only be tested *a posteriori* as a function of the results obtained for the considered nuclei.

Once the IBM parameters are determined for each Kr nucleus, the Hamiltonian $\hat{H}$ is diagonalized in the $[n_b] \oplus$

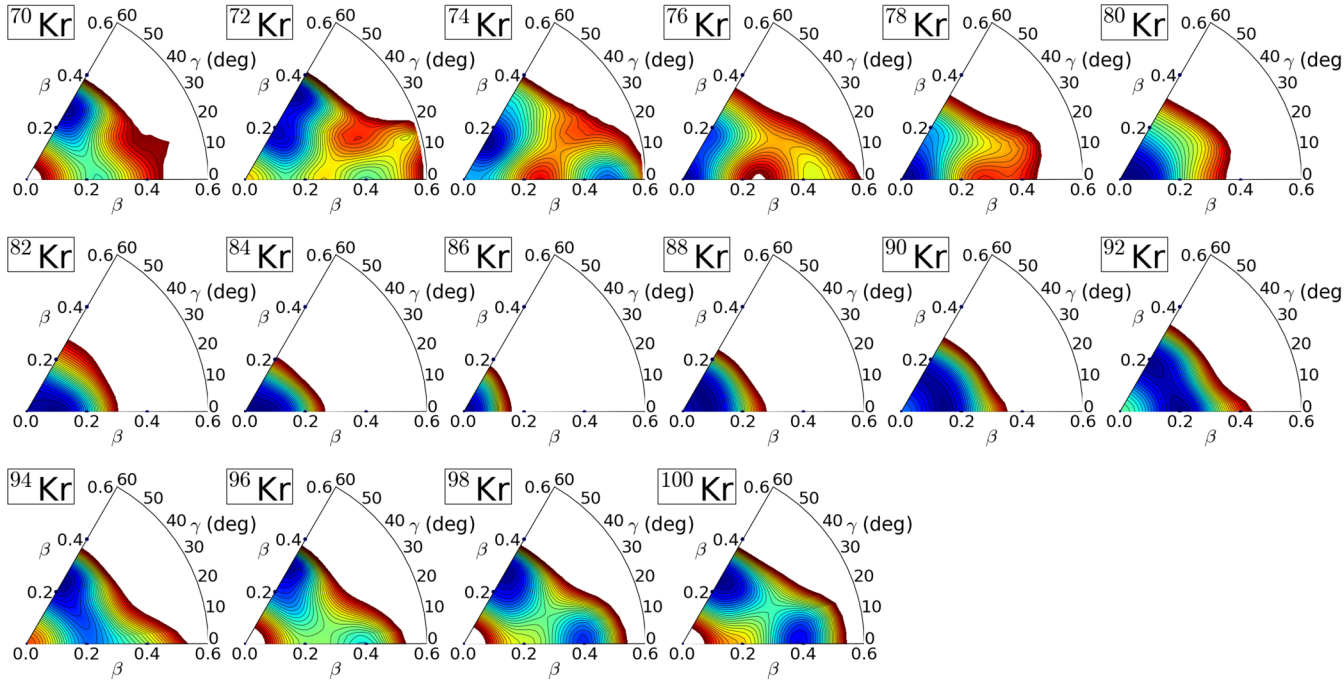

FIG. 1. SCMF (β,γ)-deformation energy surfaces for the $^{70-100}$Kr nuclei, obtained with the Gogny-D1M EDF. The energy difference between neighboring contours is 100 keV.

$[n_b+2]\oplus[n_b+4]$ space by using the code IBM-1 [52]. The IBM wave functions resulting from the diagonalization are then used to compute electromagnetic properties, including $E2$ and $E0$ transitions, that could be considered signatures of shape coexistence and shape transitions. The $B(E2)$ transition probability reads

$$B(E2;J_i\rightarrow J_f)=\frac{1}{2J_i+1}|\langle J_f||\hat{T}^{(E2)}||J_i\rangle|^2, \qquad (8)$$

where J_i and J_f are the spins of the initial and final states, respectively. iOn the other hand, the $\rho^2(E0)$ values are computed as

$$\rho^2(E0;0_i^+\rightarrow 0_f^+)=\frac{Z^2}{R_0^4}|\langle 0_f^+||\hat{T}^{(E0)}||0_i^+\rangle|^2, \qquad (9)$$

where $R_0=1.2A^{1/3}$ fm.

The $E0$ and $E2$ operators take the form $\hat{T}^{(E0)}=\sum_{n=0,1}(e^s_{0,n}\hat{n}_s+e^d_{0,n}\hat{n}_d)$ and $\hat{T}^{(E2)}=\sum_{n=0,1}e_{2,n}\hat{Q}$, respectively. For the effective charges for the E0 operator we have assumed $e^s_{0,0}=e^s_{0,1}=e^s_{0,2}\equiv e^s_0$ as well as $e^d_{0,0}=e^d_{0,1}=e^d_{0,2}\equiv e^d_0$. Also, the ratio $e^d_0/e^s_0=1.4$ has been assumed so as to obtain an overall agreement with the experimental trend of the $\rho^2(E0;0_2^+\rightarrow 0_1^+)$ values around $N=40$. The remaining parameter e^s_0 is fitted to reproduce the experimental $\rho^2(E0;0_2^+\rightarrow 0_1^+)$ value for ^{76}Kr. For the $E2$ effective charges, we have assumed the ratios $e_{2,1}/e_{2,0}=\kappa_1/\kappa_0$ and $e_{2,2}/e_{2,0}=\kappa_2/\kappa_0$, based on the fact that both the effective charge and quadrupole interaction are proportional to the mean-square proton radius [41,42]. We have then fitted the overall factor $e_{2,0}$ to the experimental $B(E2;2_1^+\rightarrow 0_1^+)$ value for ^{76}Kr [53].

III. RESULTS

In this section, we discuss the results of our calculations for the selected set of Kr isotopes. First, in Sec. III A, we discuss the (β,γ)-deformation energy surfaces obtained from the SCMF calculations as well as the mapped IBM ones. The IBM parameters derived via the mapping procedure and the configurations employed in the calculations are presented in Sec. III B. In Secs. III C and III D, we discuss spectroscopic properties such as the systematics of the energy spectra and the transition rates predicted in our calculations in comparison with the available experimental data. The detailed spectroscopy of a selected sample of Kr isotopes is discussed in Sec. III E. Finally, in Sec. III F, we consider the sensitivity of the results with respect to the underlying EDF used in the mapping procedure.

A. Deformation energy surfaces

The Gogny-D1M HFB energy surfaces are depicted in Fig. 1 for the studied $^{70-100}$Kr isotopes. In the case of ^{70}Kr, one observes an absolute oblate and a secondary prolate minima. The energy surface obtained for ^{72}Kr exhibits a complex topology with two oblate ($\beta\approx 0.2$ and $\approx$0.3) and a prolate ($\beta\approx 0.4$) minima. For ^{74}Kr, the two oblate minima ($\beta=0.04$ and 0.15) are much softer in β, while the prolate one becomes more pronounced. Thus, ^{74}Kr presents one of the best examples for the prolate-oblate shape coexistence in this region of the nuclear chart. In the case of ^{76}Kr, we find a spherical global minimum that could be associated with the neutron $N=40$ subshell closure and a very shallow oblate minimum around $\beta=0.17$. On the other hand, the prolate minimum becomes less pronounced. For the nucleus ^{78}Kr, we have obtained an

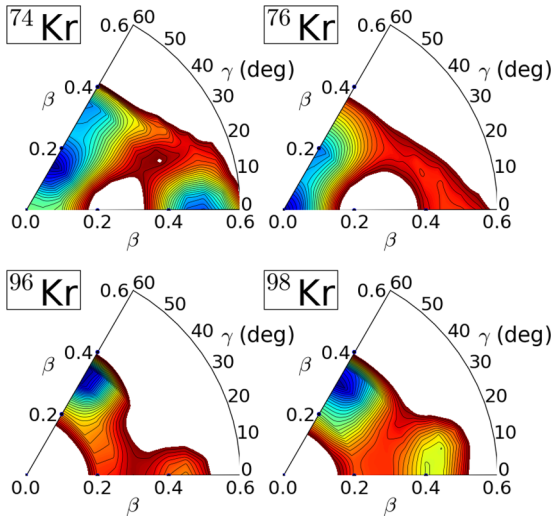

FIG. 2. The same as in Fig. 1, but for ^{74}Kr, ^{76}Kr, ^{96}Kr, and ^{98}Kr, computed with the DD-PC1 EDF.

almost invisible prolate minimum, while for $^{80–86}$Kr only a single nearly-spherical minimum is found reflecting, the effect of the $N = 50$ shell closure. On the neutron-rich side with $N > 50$, one realizes that the Gogny-D1M surfaces for $^{88–92}$Kr exhibit a pronounced γ softness, almost flat independent of γ deformation. A γ-soft oblate minimum develops for ^{94}Kr. In the case of $^{96–100}$Kr, the prolate local minimum appears at $\beta \approx 0.4$. Those nuclei exhibit a spectacular prolate-oblate shape coexistence, similarly to $^{72–76}$Kr on the neutron-deficient side.

Let us mention that similar energy surfaces have been obtained for the considered nuclei with the Gogny-D1S and D1N EDFs. However, we observe certain quantitative differences between the Gogny-D1M and the relativistic EDFs, especially for those nuclei around $N = 40$ and $N = 60$. Hence we present in Fig. 2 the SCMF energy surfaces obtained for ^{74,76}Kr and ^{96,98}Kr using relativistic Hartree-Bogoliubov calculations based on the DD-PC1 EDF. The DD-PC1 EDF provides stiffer energy surfaces with much higher barriers between the minima than the Gogny-D1M ones. We have also confirmed that there are no significant differences between the energy surfaces obtained with the relativistic DD-PC1 and DD-ME2 mean-field Lagrangians.

Finally we present in Fig. 3 the mapped IBM energy surfaces based on the Gogny-D1M ones already shown in Fig. 1. The comparison between the Gogny-D1M and IBM surfaces reveals that the latter mimic key features of the former in the neighborhood of the minima (their locations and depths, and the curvatures along the β and γ directions). As in previous works [27,28], the IBM surfaces look simpler than the mean-field ones. For instance, in the region far from each minimum the IBM surfaces become too flat. Such a discrepancy can be attributed to the simplified form of the considered IBM Hamiltonian and/or to the limited boson model space built only on the valence nucleons. Nevertheless, as will be shown later on in this paper, the low-lying collective states are determined mainly by the configurations around the minima, while the regions far from the minima are dominated by single-particle degrees of freedom. This is the reason why we have tried to reproduce the topology of the Gogny-D1M energy surfaces only in the neighborhood of the corresponding minima.

B. Configurations and derived parameters

The (β,γ) coordinates on the Gogny-D1M energy surfaces associated with the unperturbed IBM Hamiltonians of the $[n_b]$,

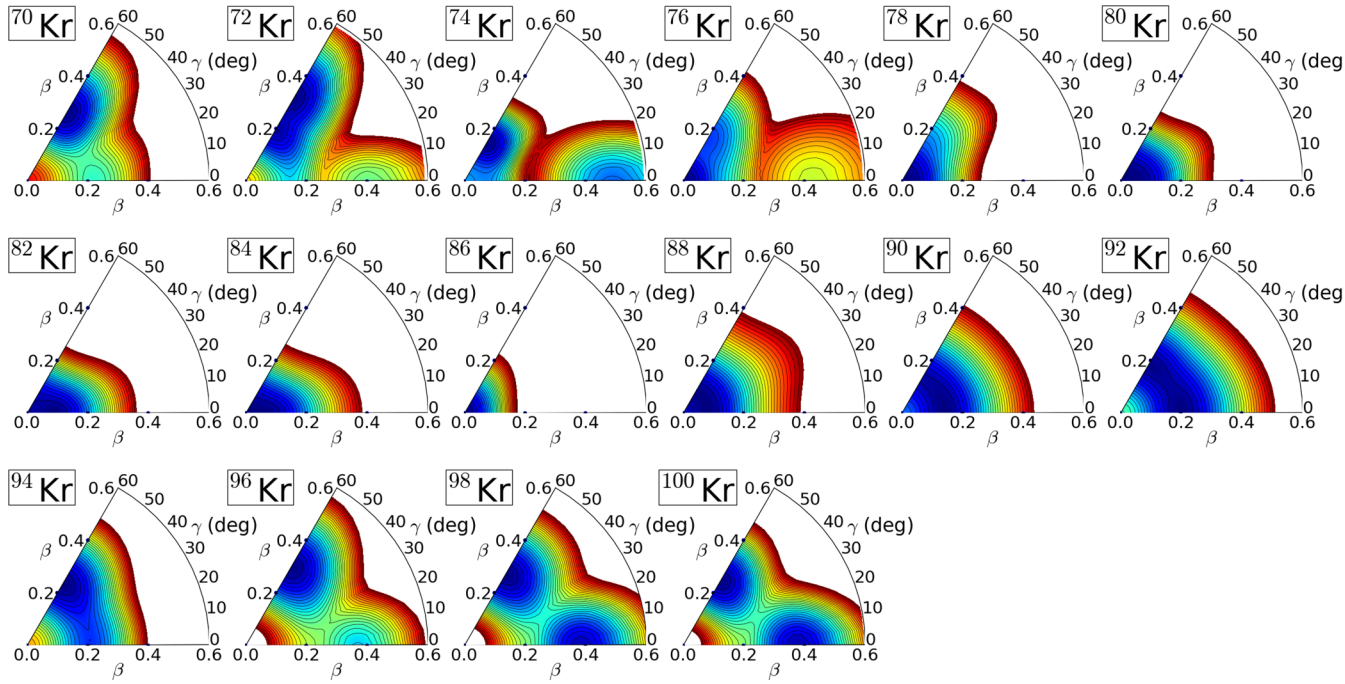

FIG. 3. The same as in Fig. 1, but for the mapped IBM energy surfaces.

TABLE I. The (β,γ) coordinates on the Gogny-D1M energy surfaces associated with the unperturbed IBM Hamiltonians in the $[n_b]$, $[n_b+2]$, and $[n_b+4]$ configurations.

	$[n_b]$	$[n_b+2]$	$[n_b+4]$
^{70}Kr	(0.26, 60°)	(0.23, 0°)	
^{72}Kr	(0.19, 60°)	(0.32, 60°)	(0.40, 0°)
^{74}Kr	(0.04, 60°)	(0.15, 60°)	(0.48, 0°)
^{76}Kr	(0.0, 0°)	(0.17, 60°)	(0.43, 0°)
^{78}Kr	(0.0, 0°)	(0.15, 60°)	
^{80}Kr	(0.04, 0°)		
^{82}Kr	(0.11, 0°)		
^{84}Kr	(0.06, 0°)		
^{86}Kr	(0.0, 0°)		
^{88}Kr	(0.08, 0°)		
^{90}Kr	(0.14, 0°)		
^{92}Kr	(0.19, 60°)	(0.21, 0°)	
^{94}Kr	(0.25, 60°)	(0.21, 0°)	
^{96}Kr	(0.31, 60°)	(0.40, 0°)	
^{98}Kr	(0.28, 60°)	(0.40, 0°)	
^{100}Kr	(0.25, 60°)	(0.38, 0°)	

$[n_b+2]$, and $[n_b+4]$ configurations are given in Table I. Let us mention that the assignment of the unperturbed configurations for ^{70}Kr and ^{94}Kr does not follow the rule mentioned in Sec. II C [step (i)]. For those nuclei, the normal $[n_b]$ configuration is assigned to the oblate minimum while the $[n_b+2]$ configuration is assigned to the prolate one with smaller β value than the former. The reason is that we assume that the intrinsic structure of each unperturbed Hamiltonian does not change too much from one nucleus to the next. As can be seen from the table, the assignment of the $[n_b]$ and $[n_b+2]$ configurations to oblate and prolate shapes in the nuclei ^{72}Kr and ^{92,96}Kr is similar to the cases of ^{70}Kr and ^{94}Kr, respectively. It is also apparent from the table that the number of configurations included in the model space differs from nucleus to nucleus. Let us stress that intruder configurations are included in our calculations depending on whether the curvatures around the HFB minimum in both β and γ directions are large enough to uniquely determine the corresponding unperturbed Hamiltonian.

The parameters of the IBM Hamiltonian (1) are plotted in Fig. 4 as functions of the neutron number N. Since, as already mentioned, the configuration space is different from nucleus to nucleus, in some Kr nuclei not all the parameters appear in the figure. For instance, values of the parameters ω [panel (e)] and Δ [panel (f)] are not plotted for those nuclei with $N = 44$–56 as the configuration mixing was not performed for them.

In the case of the unperturbed Hamiltonians [panels (a) to (d)] those parameters reflect the structural evolution along the considered isotopic chain. For example, the ϵ value for the $[n_b]$ configuration becomes larger towards the neutron subshell closure $N \approx 40$ [see panel (a)], though this is not taken into account explicitly in the model space we have employed in this study. On the other hand, the parameter κ [panel (b)] is much larger than the one employed in the IBM-1 phenomenology [54]. Such a large κ value is required to reproduce the curvature around the minimum of the Gogny-D1M energy surface.

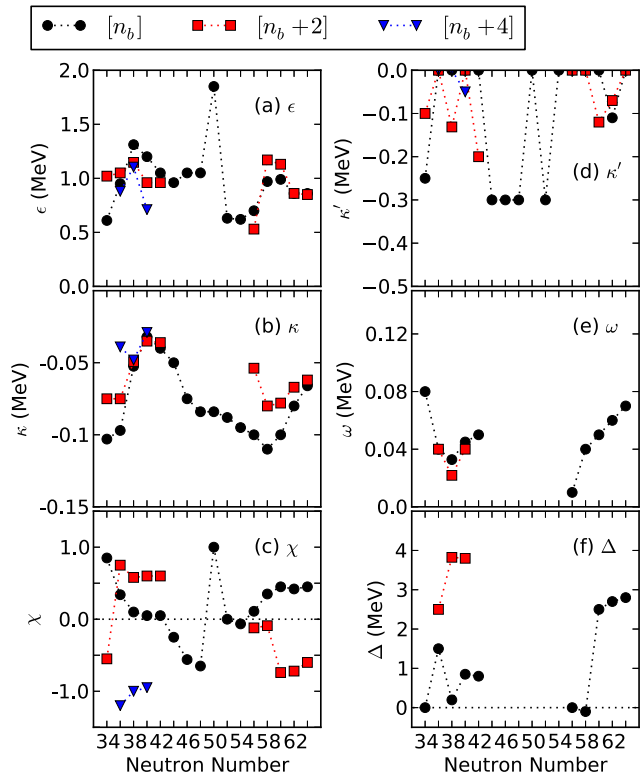

FIG. 4. Derived IBM parameters for the $[n_b]$, $[n_b+2]$, and $[n_b+4]$ configurations as functions of the neutron number.

The positive (negative) values of the parameter χ [panel (c)] correspond to oblate (prolate) shapes.

The $\hat{V}_{ddd}$ term in Eq. (3) is relevant for γ softness, as it gives rise to a triaxial minimum with $\gamma \neq 0°$ and/or 60° [43]. On the other hand, the Gogny-D1M energy surfaces in Fig. 1 suggest that none of the considered Kr nuclei exhibit a triaxial mean-field minimum. Therefore, we have assumed that the effect of this term is rather perturbative in this particular study, and the strength parameter κ' has been introduced only for those configurations corresponding to minima that are relatively soft along the γ direction so that mainly the dependence of the energy surfaces on γ is reproduced. We have also verified that the inclusion of the three-body boson term $\hat{V}_{ddd}$ improves only little the description of the energy spectra.

The behavior of the mixing strength ω [panel (e)] and the energy offset Δ [panel (f)] around $N = 36$ and 60 correspond to the significant change expected in the nuclear structure around those neutron numbers.

C. Systematics of excitation spectra

Even though the analysis of the (β,γ)-deformation energy surfaces provides useful insights into both the shape transition and shape coexistence phenomena in the studied Kr isotopes, a more quantitative analysis should go beyond the mean-field level to examine spectroscopic properties such as the excitation spectra and transition rates, which can be directly compared with the available experimental data. In this and the following Sec. III D, we turn our attention to those properties.

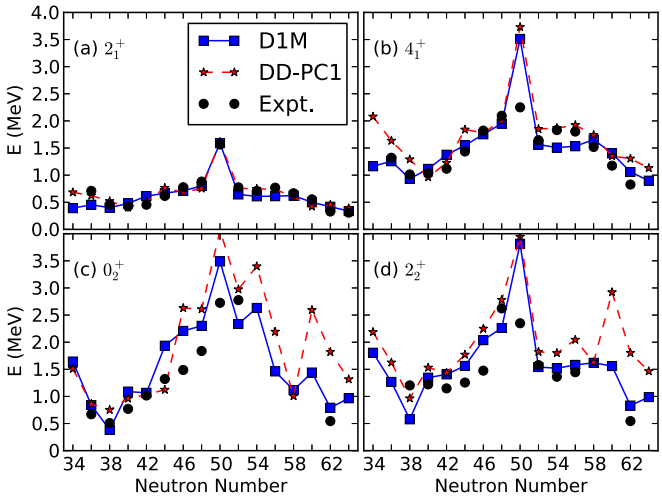

FIG. 5. Experimental [12–15,53] and computed excitation spectra for the 2_1^+, 4_1^+, 0_2^+, and 2_2^+ states in $^{70-100}$Kr as functions of N. The theoretical results are obtained with the Gogny-D1M and relativistic DD-PC1 EDFs.

The excitation energies of the 2_1^+ [panel (a)], 4_1^+ [panel (b)], 0_2^+ [panel (c)], and 2_2^+ [panel (d)] states are plotted in Fig. 5 as functions of the neutron number N. The results obtained with the parametrization D1M of the Gogny-EDF are compared with those obtained using the DD-PC1 relativistic mean-field Lagrangian as well as with the available experimental data [12–15,53]. The fraction of the three configurations $[n_b]$, $[n_b + 2]$, and $[n_b + 4]$ in the wave functions of the 0_1^+, 2_1^+, 0_2^+, and 2_2^+ states are given in Table II.

The energy spectra, computed with the D1M and DD-PC1 EDFs display a reasonable agreement with the experimental data. The $E(2_1^+)$ excitation energy can be regarded as one of the basic quantities signaling a shape/phase transition [1,2]. The predicted $E(2_1^+)$ energies, shown in panel (a) of Fig. 5, nicely follow the experimental trend though at $N = 36$ our calculations rather underestimate the experiment. Note that the lowering of the $E(2_1^+)$ towards the midshells, on both the neutron-deficient ($N \approx 40$) and the neutron-rich ($N \approx 64$) sides, signals the emergence of quadrupole collectivity. Furthermore, the decrease of the predicted $E(2_1^+)$ energies on the neutron-rich side agrees well with the smooth onset of deformation suggested by recent experiments [11,12]. Similar results are obtained for the $E(4_1^+)$ excitation energies [panel (b)]. However, they overestimate the experimental data at $N = 50$ due to the limited IBM space consisting only of s and d bosons. Those results also indicate the need of including $J^\pi = 4^+$ (or g) bosons in our calculations. Work along these lines is in progress and will be reported elsewhere.

TABLE II. Fraction (in units of percent) of the three configurations $[n_0]$, $[n_1]$, and $[n_2]$ ($n_k = n_b + 2k$) in the 0_1^+, 0_2^+, 2_1^+, and 2_2^+ wave functions of those Kr nuclei where configuration mixing has been performed in the present calculation.

	0_1^+			0_2^+			2_1^+			2_2^+		
	$[n_0]$	$[n_1]$	$[n_2]$	$[n_0]$	$[n_1]$	$[n_2]$	$[n_0]$	$[n_1]$	$[n_2]$	$[n_0]$	$[n_1]$	$[n_2]$
^{70}Kr	89	11		18	82		94	6		23	77	
^{72}Kr	58	42	0	42	58	0	43	56	0	57	43	0
^{74}Kr	5	77	18	2	17	82	2	54	44	2	44	54
^{76}Kr	23	74	3	68	28	3	12	85	4	13	68	19
^{78}Kr	56	44		44	56		42	58		49	51	
^{94}Kr	83	17		17	83		87	13		20	80	
^{96}Kr	93	7		10	90		96	4		19	81	
^{98}Kr	60	40		42	58		50	50		56	44	
^{100}Kr	32	68		68	32		21	79		79	21	

The $E(0_2^+)$ excitation energies are plotted in panel (c) of Fig. 5. As can be seen, our calculations describe fairly well the experimental data around $N = 40$ where a pronounced coexistence between oblate and prolate shapes is suggested by the corresponding Gogny-D1M energy surfaces (see Fig. 1). The predicted values overestimate the experimental ones from $N = 44$ to 50 since configuration mixing has not been performed for those nuclei. Beyond the neutron shell closure $N = 50$ one observes a lowering in the predicted energies towards $N = 64$.

The $E(0_2^+)$ values obtained with both the D1M and DD-PC1 EDFs display a peak at $N = 60$. This could be a consequence of the prolate local minimum that emerges for ^{96}Kr at $\beta \approx 0.4$ (see Fig. 1). The 0_2^+ state in this nucleus is mainly made of the prolate configuration (see Tables I and II). The Gogny-D1M result exhibits an abrupt decrease from $N = 60$ to 62, where the prolate minimum becomes much more pronounced. A similar observation can be made for the systematics of the $E(2_2^+)$ excitation energies in panel (d). In the case of the DD-PC1 EDF, higher $E(0_2^+)$ and $E(2_2^+)$ excitation energies than those obtained with the Gogny-D1M EDF are predicted for the neutron-rich Kr isotopes. This difference can be mainly attributed to the different topology of the corresponding energy surfaces. In fact, as we have already shown in Figs. 1 and 2, the DD-PC1 surfaces are generally stiffer than the D1M ones.

D. Systematics of $E2$ and $E0$ transition rates

In this section we discuss the systematics of the $B(E2)$ and $\rho^2(E0)$ transition strengths. In Fig. 6 we have plotted the experimental [4,53,55] and theoretical $B(E2; 2_1^+ \to 0_1^+)$ [panel (a)], $B(E2; 4_1^+ \to 2_1^+)$ [panel (b)], $B(E2; 0_2^+ \to 2_1^+)$ [panel (c)], and $B(E2; 2_2^+ \to 2_1^+)$ [panel (d)] transition strengths as well as the $\rho^2(E0; 0_2^+ \to 0_1^+)$ values [panel (e)], as functions of the neutron number N. Results were obtained with the Gogny-D1M and DD-PC1 EDFs.

The $B(E2; 2_1^+ \to 0_1^+)$ and $B(E2; 4_1^+ \to 2_1^+)$ transition probabilities agree reasonably well with the experimental data. They display the well-known systematics signaling the development of collectivity; i.e., they increase when departing from the shell closure and become maximal around midshell. On the other hand, the $B(E2; 0_2^+ \to 2_1^+)$ transition probabilities can be regarded as a measure of shape mixing. As can be seen from panel (c), the $B(E2; 0_2^+ \to 2_1^+)$ values, obtained with both the D1M and DD-PC1 EDFs, exhibit a peak around $N = 40$ where the corresponding mean-field energy surfaces display coexisting minima and their mixing is expected to be strong. However, the theoretical $B(E2; 0_2^+ \to 2_1^+)$ values for ^{74,76}Kr

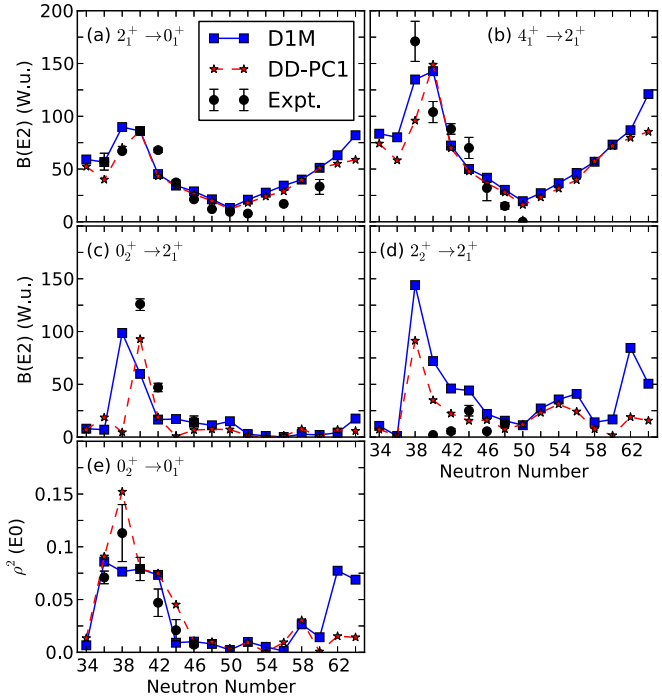

FIG. 6. The experimental [4,53,55] and theoretical $B(E2;2_1^+ \to 0_1^+)$ (a), $B(E2;4_1^+ \to 2_1^+)$ (b), $B(E2;0_2^+ \to 2_1^+)$ (c), and $B(E2;2_2^+ \to 2_1^+)$ (d) transition strengths (in Weisskopf units), and $\rho^2(E0;0_2^+ \to 0_1^+)$ values for the $^{70-100}$Kr nuclei depicted as functions of the neutron number. The theoretical calculations were performed based on the Gogny-D1M and relativistic DD-PC1 EDFs.

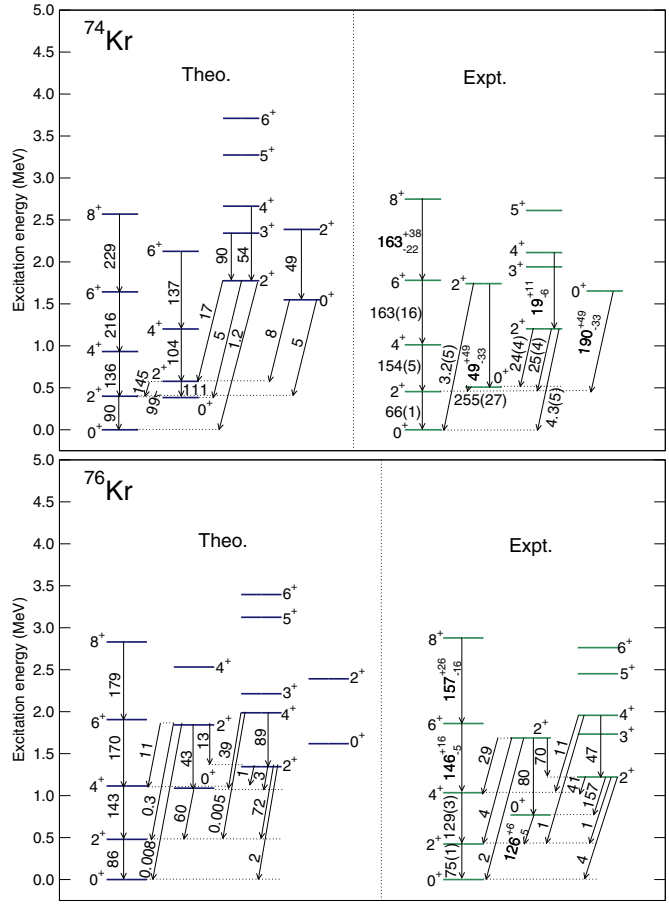

FIG. 7. The theoretical low-energy excitation spectra and $B(E2)$ transition strengths (in W.u., indicated by along arrows) of the ^{74}Kr and ^{76}Kr isotopes obtained from the Gogny-D1M EDF, in comparison to the available experimental data [4,53].

considerably underestimate the experimental ones [4]. Note that the experimental value $B(E2;0_2^+ \to 2_1^+) = 255 \pm 27$ W.u [4] for ^{74}Kr is too large compared to the one obtained in our calculations and, therefore, is not shown in the figure. This is due to the fact (see Table II) that the compositions of the 0_2^+ and 2_1^+ IBM wave functions are rather different. Furthermore, the small $B(E2;0_2^+ \to 2_1^+)$ values obtained for neutron-rich Kr isotopes indicate that there is almost no mixing between the 0_2^+ and 2_1^+ states. A pronounced difference between the D1M and DD-PC1 EDFs is observed in the case of ^{74}Kr for which the $B(E2;0_2^+ \to 2_1^+)$ value obtained with the latter is almost zero. As can be seen from Figs. 1 and 2, the DD-PC1 energy surface for ^{74}Kr displays three minima within 1 MeV a structure, more complex than the corresponding Gogny-D1M one. Therefore, the IBM Hamiltonian used in this study seems to be too simple to account for the large experimental $B(E2;0_2^+ \to 2_1^+)$ value.

Experimental data are also available for the $B(E2;2_2^+ \to 2_1^+)$ transition probability. They are depicted in panel (d) of Fig. 6. Our calculations, with both the Gogny-D1M and DD-PC1 EDFs, follow the experimental trend from $N = 44$ to 50. However, they overestimate the experimental values for ^{76,78}Kr. As can be seen from Table II, the 2_1^+ and 2_2^+ wave functions for those nuclei have a similar structure, leading to large $E2$ matrix elements.

Finally, another signature of shape coexistence is provided by the $\rho^2(E0;0_2^+ \to 0_1^+)$ values [3]. They are compared in panel (e) with the experiment [55]. Both the experimental and theoretical $\rho^2(E0;0_2^+ \to 0_1^+)$ values are notably large around $N = 38$–40, signalling the shape coexistence in those isotopes. Note that, regardless of the considered EDF, the agreement with the experimental data is rather good.

E. Detailed spectroscopy of selected isotopes

We now turn our attention to a more detailed analysis of the low-energy spectroscopy of individual nuclei. To this end, we consider the neutron-deficient ^{74,76}Kr and the neutron-rich ^{96,98}Kr isotopes that exhibit a pronounced shape coexistence. The corresponding IBM states have been grouped into bands according to the dominant $E2$ decay patterns.

The Gogny-D1M energy surfaces for ^{74,76}Kr display coexisting spherical, oblate and prolate minima (see Fig. 1). One of the most remarkable features of the spectra obtained for those nuclei is the presence of low-lying 0_2^+ states (see Fig. 5). As can be seen from Fig. 7, the low-energy excitation spectra obtained for ^{74,76}Kr, with the Gogny-D1M EDF, agree reasonably well with the experimental ones [4]. In our calculations, the 0_1^+ ground states for both ^{74,76}Kr are mainly oblate in nature while the 0_2^+ states are predominantly prolate and spherical, respectively (see Tables I and II). In the case of ^{74}Kr, our calculations suggest rather large interband $B(E2)$

transitions between the lowest-spin states of the ground-state and the first excited bands. This is confirmed by the strong $B(E2;0_2^+ \to 2_1^+)$ and $B(E2;2_2^+ \to 2_1^+)$ values, which are about the same order of magnitude as the $B(E2;2_1^+ \to 0_1^+)$ rate. Note, however, that the predicted $B(E2;0_2^+ \to 2_1^+)$ value accounts for only half the experimental one [4]. As already mentioned above, this disagreement suggests that a much stronger mixing between those states would be necessary to reproduce the large experimental $B(E2;0_2^+ \to 2_1^+)$ transition probability. Previous five-dimensional collective Hamiltonian (5DCH) calculations [6] based on the relativistic PC-PK1 EDF also underestimate the strong $B(E2;0_2^+ \to 2_1^+)$ rate for ^{74}Kr. On the other hand, the 5DCH calculations based on the Gogny-D1S EDF [4] account for it. Our results also suggest that in the case of ^{74}Kr the quasi-γ band is built on the 2_3^+ state. The computed 0_3^+ excitation energy agrees well with the experimental result whereas the $B(E2;0_3^+ \to 2_1^+)$ value is too small compared to the latter.

As shown in the lower panel of Fig. 7, our calculations provide a reasonable agreement with the experimental data for ^{76}Kr. However, as in the case of ^{74}Kr, they underestimate the $B(E2;0_2^+ \to 2_1^+)$ transition strength. Note, that the theoretical 3^+ and 4^+ levels in the quasi-γ band, i.e., the second excited band built on the 2_3^+ state, of ^{76}Kr are reversed. This might be a consequence of the strong level repulsion among the 4^+ states due to configuration mixing.

In Fig. 8, we have plotted the low-energy excitation spectra for the neutron-rich nuclei ^{96,98}Kr, which exhibit spectacular coexistence between prolate and oblate shapes (see Fig. 1). As can be seen from Tables I and II, for both nuclei the 0_1^+ and 0_2^+ states are mainly arising from the oblate and prolate configurations, respectively, while the two configurations are more strongly mixed in ^{98}Kr than in ^{96}Kr. The predicted level schemes for both nuclei look rather similar and reproduce the experimental systematics [12,14,15] for the lowest-lying states.

Note that the level of accuracy of our results in describing the low-energy spectra shown in Figs. 7 and 8 is comparable with that of the recent symmetry-projected GCM calculation, based on the Gogny-D1S EDF, in which the triaxial deformation was included as a generating coordinate [7]. In Ref. [7], similar low-energy band structure to ours was obtained for ^{74,76}Kr as well as for ^{96,98}Kr. The energy spectra for ^{96,98}Kr in the present calculation, however, generally look more stretched than those obtained in Ref. [7].

F. Sensitivity test

Among the various factors that could affect the spectroscopic properties obtained for the studied nuclei, the choice of the EDF at the mean-field level is a relevant one since the parameters of the IBM Hamiltonian are determined as so to reproduce the topology of the SCMF energy surfaces. In this section, we analyze the sensitivity of the calculated excitation spectra with respect to the choice of the underlying EDF. To this end, in Fig. 9, we have compared the low-energy excitation spectra obtained for ^{76}Kr (upper panel) and ^{98}Kr (lower panel). Calculations have been carried out with three different parametrizations of the Gogny-EDF, i.e., D1S [30],

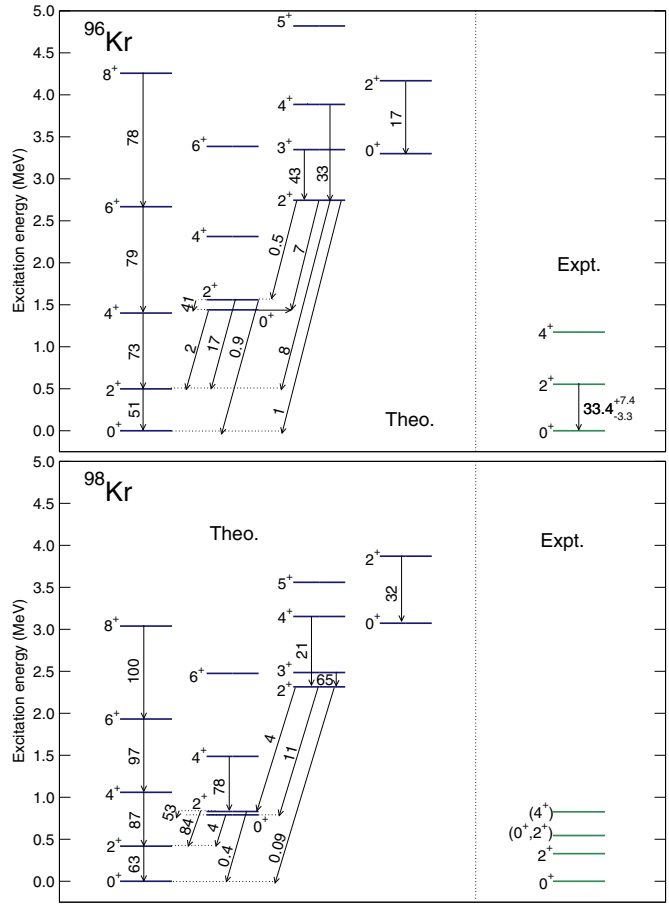

FIG. 8. The same as in Fig. 7, but for ^{96}Kr and ^{98}Kr. The experimental data were taken from Refs. [12,14,15].

D1M [29], and D1N [31], as well as with two parametrizations of the relativistic mean-field Lagrangian, i.e., DD-ME2 [32] and DD-PC1 [33]. The experimental data are also included in the plots. As can be seen from the figure, all the EDFs provide similar excitation spectra for ^{76}Kr. On the other hand, in the case of ^{98}Kr, the spectra obtained with the three Gogny EDFs are rather similar while there are significant differences with the ones provided by the DD-ME2 and DD-PC1 parameter sets, which provide much more stretched energy levels, particularly for the non-yrast states.

IV. SUMMARY AND PERSPECTIVES

In this paper, we have studied the shape transition and shape coexistence phenomena along the Kr isotopic chain. To this end, the nuclei $^{70-100}$Kr have been taken as an illustrative sample. We have resorted to a fermion-to-boson mapping procedure based on mapping the fermionic (β,γ) energy contour plot onto the expectation value of the IBM Hamiltonian that includes configuration mixing. The parameters of the IBM Hamiltonian have been determined through this procedure and used to compute spectroscopic properties that characterize the structural evolution along the Kr isotopic chain. The microscopic input to our calculations is provided by SCMF calculations based on the nonrelativistic Gogny-EDF as

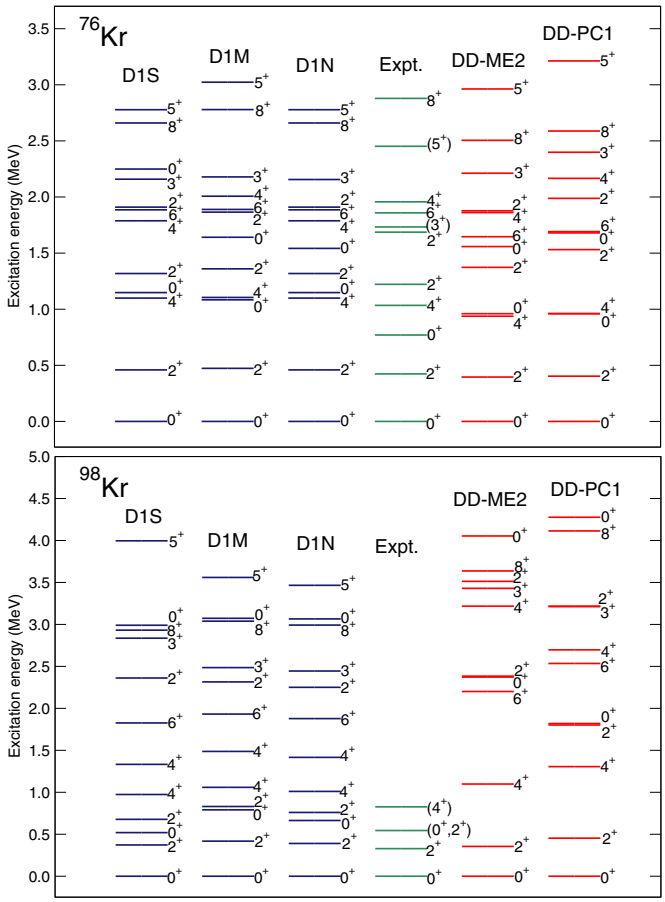

FIG. 9. Comparison of the low-energy excitation spectra obtained for ^{76}Kr and ^{98}Kr with the Gogny D1S, D1M, and D1N EDFs as well as with the relativistic DD-ME2 and DD-PC1 EDFs. The corresponding experimental spectra are also included in the plot.

well as different parametrizations of the relativistic mean-field Lagrangian. In particular, for the former we have considered the three parameter sets D1S, D1N, and D1M while for the latter we have considered the DD-ME2 and DD-PC1 parametrizations.

The Gogny-D1M energy surfaces suggest an oblate ground state for ^{70}Kr, coexisting oblate and prolate minima in the case of ^{72,74}Kr, and spherical-oblate-prolate triple shape coexistence for ^{76,78}Kr. On the other hand, nearly spherical ground states are found for $^{80–86}$Kr while γ-softness emerges in the case of ^{88,90,92}Kr. An oblate ground state is predicted for ^{94}Kr. Moreover, prolate-oblate shape coexistence is obtained for the heavier nuclei ^{96,98,100}Kr.

The evolution of the low-energy excitation spectra, $B(E2)$ transition rates, and the $\rho^2(E0)$ values, as functions of the neutron number, correlates well with the systematics of the Gogny-D1M energy surfaces. Despite the simplicity of the considered (mapped) IBM approach, the predicted spectroscopic properties exhibit a reasonable agreement with the available experimental data. We have also studied the robustness of our approach by comparing the excitation spectra obtained from several nonrelativistic and relativistic EDFs. Such a comparison reveals no essential difference between the predictions obtained for neutron-deficient Kr isotopes. On the other hand, we have found that the relativistic and nonrelativistic EDFs provide notably different predictions in the case of neutron-rich systems.

Several approximations have been made at various levels of the mapping procedure. This leads to a disagreement with the experimental data in some spectroscopic properties. For example, near $N = 40$ our approach does not reproduce the interband $B(E2; 0_2^+ \to 2_1^+)$ and $B(E2; 2_2^+ \to 2_1^+)$ transitions. Therefore, further improvement of our mapping procedure is still required to properly account for shape mixing. A similar conclusion has been reached in our previous studies of nuclei in this region of the nuclear chart [27,28] regardless of the underlying EDF employed in the mapping procedure. A possible improvement would be to use a more general form of the IBM Hamiltonian that includes additional degrees of freedom like proton and neutron bosons. This, however, would increase the number of parameters in our model. Those parameters could not be uniquely determined just by looking at the (static) mean-field energy surfaces, and additional microscopic input would be needed for the mapping procedure.

Another example is the assumption on the IBM configuration space. We have associated the particle-hole configurations with the mean-field minima with larger β deformation. This assumption, however, may not obviously provide a proper interpretation of coexisting shapes in the considered Kr nuclei. In addition, while we have considered only the proton particle-hole excitations across the $Z = 28$ shell gap as the source of shape coexistence, there could be some other possibilities of particle-hole excitations, e.g., those of neutrons especially around the subshell closure $N = 40$. Therefore, in order to associate a configuration to each mean-field minimum in a more unambiguous manner, a more elaborate analysis would be required to examine the nature of the underlying SCMF state at each minimum to see which particle-hole components play a role, and then incorporate it into the corresponding boson subspace. Such an analysis would require another extensive study with further complications arising, e.g., from the inclusion of additional boson degrees of freedom, which is well beyond the scope of the present work. Work along these lines represents an important step for further developing our mapping procedure and will be considered in future studies.

ACKNOWLEDGMENTS

K.N. acknowledges support from the Japan Society for the Promotion of Science. This work has been supported in part by the QuantiXLie Centre of Excellence. The work of LMR was supported by Spanish Ministry of Economy and Competitiveness (MINECO) Grants No. FPA2015-65929-P and No. FIS2015-63770-P.

[1] R. F. Casten, *Nuclear Structure from a Simple Perspective* (Oxford University Press, Oxford, 2005).

[2] P. Cejnar, J. Jolie, and R. F. Casten, Rev. Mod. Phys. **82**, 2155 (2010).

[3] K. Heyde and J. L. Wood, Rev. Mod. Phys. **83**, 1467 (2011).
[4] E. Clément, A. Görgen, W. Korten, E. Bouchez, A. Chatillon, J.-P. Delaroche, M. Girod, H. Goutte, A. Hürstel, Y. Le Coz, A. Obertelli, S. Péru, C. Theisen, J. N. Wilson, M. Zielińska, C. Andreoiu, F. Becker, P. A. Butler, J. M. Casandjian, W. N. Catford, T. Czosnyka, G. de France, J. Gerl, R.-D. Herzberg, J. Iwanicki, D. G. Jenkins, G. D. Jones, P. J. Napiorkowski, G. Sletten, and C. N. Timis, Phys. Rev. C **75**, 054313 (2007).
[5] M. Bender, P. Bonche, and P.-H. Heenen, Phys. Rev. C **74**, 024312 (2006).
[6] Y. Fu, H. Mei, J. Xiang, Z. P. Li, J. M. Yao, and J. Meng, Phys. Rev. C **87**, 054305 (2013).
[7] T. R. Rodríguez, Phys. Rev. C **90**, 034306 (2014).
[8] A. Petrovici, K. Schmid, and A. Faessler, Nucl. Phys. A **665**, 333 (2000).
[9] K. Sato and N. Hinohara, Nucl. Phys. A **849**, 53 (2011).
[10] S. Naimi, G. Audi, D. Beck, K. Blaum, C. Böhm, C. Borgmann, M. Breitenfeldt, S. George, F. Herfurth, A. Herlert, M. Kowalska, S. Kreim, D. Lunney, D. Neidherr, M. Rosenbusch, S. Schwarz, L. Schweikhard, and K. Zuber, Phys. Rev. Lett. **105**, 032502 (2010).
[11] M. Albers, N. Warr, K. Nomura, A. Blazhev, J. Jolie, D. Mücher, B. Bastin, C. Bauer, C. Bernards, L. Bettermann, V. Bildstein, J. Butterworth, M. Cappellazzo, J. Cederkäll, D. Cline, I. Darby, S. Das Gupta, J. M. Daugas, T. Davinson, H. De Witte, J. Diriken, D. Filipescu, E. Fiori, C. Fransen, L. P. Gaffney, G. Georgiev, R. Gernhäuser, M. Hackstein, S. Heinze, H. Hess, M. Huyse, D. Jenkins, J. Konki, M. Kowalczyk, T. Kröll, R. Krücken, J. Litzinger, R. Lutter, N. Marginean, C. Mihai, K. Moschner, P. Napiorkowski, B. S. Nara Singh, K. Nowak, T. Otsuka, J. Pakarinen, M. Pfeiffer, D. Radeck, P. Reiter, S. Rigby, L. M. Robledo, R. Rodríguez-Guzmán, M. Rudigier, P. Sarriguren, M. Scheck, M. Seidlitz, B. Siebeck, G. Simpson, P. Thöle, T. Thomas, J. Van de Walle, P. Van Duppen, M. Vermeulen, D. Voulot, R. Wadsworth, F. Wenander, K. Wimmer, K. O. Zell, and M. Zielinska, Phys. Rev. Lett. **108**, 062701 (2012).
[12] M. Albers, K. Nomura, N. Warr, A. Blazhev, J. Jolie, D. Mücher, B. Bastin, C. Bauer, C. Bernards, L. Bettermann, V. Bildstein, J. Butterworth, M. Cappellazzo, J. Cederkäll, D. Cline, I. Darby, S. D. Gupta, J. Daugas, T. Davinson, H. D. Witte, J. Diriken, D. Filipescu, E. Fiori, C. Fransen, L. Gaffney, G. Georgiev, R. Gernhäuser, M. Hackstein, S. Heinze, H. Hess, M. Huyse, D. Jenkins, J. Konki, M. Kowalczyk, T. Kröll, R. Krücken, J. Litzinger, R. Lutter, N. Marginean, C. Mihai, K. Moschner, P. Napiorkowski, B. N. Singh, K. Nowak, J. Pakarinen, M. Pfeiffer, D. Radeck, P. Reiter, S. Rigby, L. Robledo, R. Rodríguez-Guzmán, M. Rudigier, M. Scheck, M. Seidlitz, B. Siebeck, G. Simpson, P. Thöle, T. Thomas, J. V. de Walle, P. V. Duppen, M. Vermeulen, D. Voulot, R. Wadsworth, F. Wenander, K. Wimmer, K. Zell, and M. Zielinska, Nucl. Phys. A **899**, 1 (2013).
[13] T. Rzaca-Urban, K. Sieja, W. Urban, M. Czerwiński, A. Blanc, M. Jentschel, P. Mutti, U. Köster, T. Soldner, G. de France, G. S. Simpson, and C. A. Ur, Phys. Rev. C **95**, 064302 (2017).
[14] J. Dudouet, A. Lemasson, G. Duchêne, M. Rejmund, E. Clément, C. Michelagnoli, F. Didierjean, A. Korichi, G. Maquart, O. Stezowski, C. Lizarazo, R. M. Pérez-Vidal, C. Andreoiu, G. de Angelis, A. Astier, C. Delafosse, I. Deloncle, Z. Dombradi, G. de France, A. Gadea, A. Gottardo, B. Jacquot, P. Jones, T. Konstantinopoulos, I. Kuti, F. Le Blanc, S. M. Lenzi, G. Li, R. Lozeva, B. Million, D. R. Napoli, A. Navin, C. M. Petrache, N. Pietralla, D. Ralet, M. Ramdhane, N. Redon, C. Schmitt, D. Sohler, D. Verney, D. Barrientos, B. Birkenbach, I. Burrows, L. Charles, J. Collado, D. M. Cullen, P. Désesquelles, C. Domingo Pardo, V. González, L. Harkness-Brennan, H. Hess, D. S. Judson, M. Karolak, W. Korten, M. Labiche, J. Ljungvall, R. Menegazzo, D. Mengoni, A. Pullia, F. Recchia, P. Reiter, M. D. Salsac, E. Sanchis, C. Theisen, J. J. Valiente-Dobón, and M. Zielińska, Phys. Rev. Lett. **118**, 162501 (2017).
[15] F. Flavigny, P. Doornenbal, A. Obertelli, J.-P. Delaroche, M. Girod, J. Libert, T. R. Rodriguez, G. Authelet, H. Baba, D. Calvet, F. Château, S. Chen, A. Corsi, A. Delbart, J.-M. Gheller, A. Giganon, A. Gillibert, V. Lapoux, T. Motobayashi, M. Niikura, N. Paul, J.-Y. Roussé, H. Sakurai, C. Santamaria, D. Steppenbeck, R. Taniuchi, T. Uesaka, T. Ando, T. Arici, A. Blazhev, F. Browne, A. Bruce, R. Carroll, L. X. Chung, M. L. Cortés, M. Dewald, B. Ding, S. Franchoo, M. Górska, A. Gottardo, A. Jungclaus, J. Lee, M. Lettmann, B. D. Linh, J. Liu, Z. Liu, C. Lizarazo, S. Momiyama, K. Moschner, S. Nagamine, N. Nakatsuka, C. Nita, C. R. Nobs, L. Olivier, R. Orlandi, Z. Patel, Z. Podolyák, M. Rudigier, T. Saito, C. Shand, P. A. Söderström, I. Stefan, V. Vaquero, V. Werner, K. Wimmer, and Z. Xu, Phys. Rev. Lett. **118**, 242501 (2017).
[16] T. Togashi, Y. Tsunoda, T. Otsuka, and N. Shimizu, Phys. Rev. Lett. **117**, 172502 (2016).
[17] C. Kremer, S. Aslanidou, S. Bassauer, M. Hilcker, A. Krugmann, P. von Neumann-Cosel, T. Otsuka, N. Pietralla, V. Y. Ponomarev, N. Shimizu, M. Singer, G. Steinhilber, T. Togashi, Y. Tsunoda, V. Werner, and M. Zweidinger, Phys. Rev. Lett. **117**, 172503 (2016).
[18] E. Clément, M. Zielińska, S. Péru, H. Goutte, S. Hilaire, A. Görgen, W. Korten, D. T. Doherty, B. Bastin, C. Bauer, A. Blazhev, N. Bree, B. Bruyneel, P. A. Butler, J. Butterworth, J. Cederkäll, P. Delahaye, A. Dijon, A. Ekström, C. Fitzpatrick, C. Fransen, G. Georgiev, R. Gernhäuser, H. Hess, J. Iwanicki, D. G. Jenkins, A. C. Larsen, J. Ljungvall, R. Lutter, P. Marley, K. Moschner, P. J. Napiorkowski, J. Pakarinen, A. Petts, P. Reiter, T. Renstrøm, M. Seidlitz, B. Siebeck, S. Siem, C. Sotty, J. Srebrny, I. Stefanescu, G. M. Tveten, J. Van de Walle, M. Vermeulen, D. Voulot, N. Warr, F. Wenander, A. Wiens, H. De Witte, and K. Wrzosek-Lipska, Phys. Rev. C **94**, 054326 (2016).
[19] E. Caurier, G. Martínez-Pinedo, F. Nowacki, A. Poves, and A. P. Zuker, Rev. Mod. Phys. **77**, 427 (2005).
[20] M. Bender, P.-H. Heenen, and P.-G. Reinhard, Rev. Mod. Phys. **75**, 121 (2003).
[21] D. Vretenar, A. V. Afanasjev, G. Lalazissis, and P. Ring, Phys. Rep. **409**, 101 (2005).
[22] T. Nikšić, D. Vretenar, and P. Ring, Prog. Part. Nucl. Phys. **66**, 519 (2011).
[23] R. Rodríguez-Guzmán, J. L. Egido, and L. M. Robledo, Nucl. Phys. A **709**, 201 (2002).
[24] J.-P. Delaroche, M. Girod, J. Libert, H. Goutte, S. Hilaire, S. Péru, N. Pillet, and G. F. Bertsch, Phys. Rev. C **81**, 014303 (2010).
[25] K. Nomura, N. Shimizu, and T. Otsuka, Phys. Rev. Lett. **101**, 142501 (2008).
[26] P. Ring and P. Schuck, *The Nuclear Many-Body Problem* (Springer-Verlag, Berlin, 1980).
[27] K. Nomura, R. Rodríguez-Guzmán, and L. M. Robledo, Phys. Rev. C **94**, 044314 (2016).
[28] K. Nomura, R. Rodríguez-Guzmán, and L. M. Robledo, Phys. Rev. C **95**, 064310 (2017).

[29] S. Goriely, S. Hilaire, M. Girod, and S. Péru, Phys. Rev. Lett. **102**, 242501 (2009).
[30] J. F. Berger, M. Girod, and D. Gogny, Nucl. Phys. A **428**, 23 (1984).
[31] F. Chappert, M. Girod, and S. Hilaire, Phys. Lett. B **668**, 420 (2008).
[32] G. A. Lalazissis, T. Nikšić, D. Vretenar, and P. Ring, Phys. Rev. C **71**, 024312 (2005).
[33] T. Nikšić, D. Vretenar, and P. Ring, Phys. Rev. C **78**, 034318 (2008).
[34] R. Rodríguez-Guzmán, P. Sarriguren, L. M. Robledo, and J. E. García-Ramos, Phys. Rev. C **81**, 024310 (2010).
[35] A. Bohr and B. M. Mottelsson, *Nuclear Structure*, Vol. 2 (Benjamin, New York, 1975), p. 45.
[36] F. Iachello and A. Arima, *The Interacting Boson Model* (Cambridge University Press, Cambridge, 1987).
[37] T. Otsuka, A. Arima, and F. Iachello, Nucl. Phys. A **309**, 1 (1978).
[38] U. Kaup and A. Gelberg, Z. Phys. A **293**, 311 (1979).
[39] P. Duval, D. Goutte, and M. Vergnes, Phys. Lett. B **124**, 297 (1983).
[40] E. Padilla-Rodal, O. Castanos, R. Bijker, and A. Galindo-Uribarri, Rev. Mex. Fis. S **52**, 57 (2006).
[41] P. D. Duval and B. R. Barrett, Phys. Lett. B **100**, 223 (1981).
[42] P. D. Duval and B. R. Barrett, Nucl. Phys. A **376**, 213 (1982).
[43] P. Van Isacker and J.-Q. Chen, Phys. Rev. C **24**, 684 (1981).
[44] K. Nomura, N. Shimizu, D. Vretenar, T. Nikšić, and T. Otsuka, Phys. Rev. Lett. **108**, 132501 (2012).
[45] A. Frank, P. Van Isacker, and C. E. Vargas, Phys. Rev. C **69**, 034323 (2004).
[46] K. Nomura, N. Shimizu, and T. Otsuka, Phys. Rev. C **81**, 044307 (2010).
[47] K. Nomura, R. Rodríguez-Guzmán, L. M. Robledo, and N. Shimizu, Phys. Rev. C **86**, 034322 (2012).
[48] K. Nomura, R. Rodríguez-Guzmán, and L. M. Robledo, Phys. Rev. C **87**, 064313 (2013).
[49] R. Bengtsson, T. Bengtsson, J. Dudek, G. Leander, W. Nazarewicz, and J. ye Zhang, Phys. Lett. B **183**, 1 (1987).
[50] R. Bengtsson and W. Nazarewicz, Z. Phys. A **334**, 269 (1989).
[51] W. Nazarewicz, Phys. Lett. B **305**, 195 (1993).
[52] P. Van Isacker, Computer program IBM-1 (unpublished).
[53] Brookhaven National Nuclear Data Center, http://www.nndc.bnl.gov.
[54] H.-B. Bai, X.-W. Li, L.-J. Lu, H.-F. Dong, Y. Wang, and J.-F. Zhang, Chin. Phys. C **40**, 074103 (2016).
[55] T. Kibédi and R. Spear, At. Data Nucl. Data Tables **89**, 77 (2005).